AAAS
Research
Volume 2018, Article ID 6914626, 9 pages
https://doi.org/10.1155/2018/6914626

Research
OFFICIAL JOURNAL OF CAST

Research Article

Rechargeable Na-CO_2 Batteries Starting from Cathode of Na_2CO_3 and Carbon Nanotubes

Jianchao Sun, Yong Lu, Hao Yang, Mo Han, Lianyi Shao, and Jun Chen*

Key Laboratory of Advanced Energy Materials Chemistry (Ministry of Education), College of Chemistry, Nankai University, Tianjin 300071, China

*Correspondence should be addressed to Jun Chen; chenabc@nankai.edu.cn

Received 22 March 2018; Accepted 3 July 2018; Published 22 August 2018

Copyright © 2018 Jianchao Sun et al. Exclusive Licensee Science and Technology Review Publishing House. Distributed under a Creative Commons Attribution License (CC BY 4.0).

Na-CO_2 batteries have attracted significant attentions due to their high energy density and effective utilization of greenhouse gas CO_2. However, all reported Na-CO_2 batteries employ excessive preloaded metal Na, which will lead to safety issues such as dendrite formation and short circuit. In addition, the charging mechanism of reported Na-CO_2 batteries is not very clear. Here we report the Na-CO_2 batteries, starting from the cathode of cheap Na_2CO_3 and multiwalled carbon nanotubes (CNTs). Due to the effective electron transfer and high reactivity, the decomposition of Na_2CO_3 and CNTs could take place under 3.8 V. The charging mechanism of $2Na_2CO_3 + C \longrightarrow 4Na + 3CO_2$ without any side reactions is revealed by in/ex situ techniques such as Raman, gas chromatograph, and optical microscope. Dendrite-free Na can quantitatively deposit on the Super P/Al anode because of large specific surface area and low nucleation barrier of the anode for Na plating. The batteries could deliver an energy density of 183 Wh kg^{-1} (based on the whole mass of the pouch-type batteries, 4 g) with stable cycling performance. This work reveals that safe rechargeable Na-CO_2 batteries could be constructed by cheap Na_2CO_3 and multiwalled carbon nanotubes.

1. Introduction

Rechargeable Na-CO_2 batteries have attracted a lot of interests because they can reuse the greenhouse gas CO_2 to realize energy storage and conversion [1–4]. The reported rechargeable Na-CO_2 batteries with liquid or quasi-solid state electrolyte employed metal Na and CO_2 as the reactants. The discharge reaction can be described by $4Na + 3CO_2 \longrightarrow 2Na_2CO_3 + C$ [3, 4]. However, Na-CO_2 batteries still suffer from safety issues and self-discharge due to the use of excessive preloaded metal Na as anode. Metal Na would encounter dendrite formation or surface cracks during cycling process due to the uneven deposition of Na, leading to short circuit [5–7]. By contrast with metal Na, Na_2CO_3 and carbon are more stable, safer, and easier to get [8]. More importantly, the generated metal Na by the charging decomposition of Na_2CO_3 and carbon is stoichiometric. The batteries with stoichiometric metal Na will be safer than that with excessive preloaded metal Na. Therefore, designing dendrite-free rechargeable Na-CO_2 batteries without preloaded metal Na is of great significance.

Due to its insulating properties, the decomposition of Na_2CO_3 will result in large polarization and inevitable side reactions such as electrolyte decomposition [9–11]. Thus, to develop rechargeable Na-CO_2 batteries starting with Na_2CO_3 and carbon, the main issue is how to realize the decomposition of Na_2CO_3 and carbon under proper voltage range. To ensure fast kinetics such as effective electron transfer during the decomposition process, Na_2CO_3 should be evenly intertwined with highly conductive carbon and the particle size should be small [12–17]. Meanwhile, the reactivity of carbon materials also has a great influence on the decomposition process [18–21]. Furthermore, the decomposition mechanism of Na_2CO_3 and carbon in previous works is not very clear [3, 4]. It is also important to find out the source of CO_2 in the charge process. In addition, to ensure Na metal is produced during charging and the generated stoichiometric metal Na does not form dendrite is also challenging [22–24].

Here we report Na-CO_2 batteries with Na-free architecture, which operate in pure CO_2 atmosphere (1 atm) (Figure 1(a)). The cathode is composed of Na_2CO_3 and CNTs (multiwalled carbon nanotubes) with defects, where stick-shaped Na_2CO_3 (about 200-300 nm in length) are intertwined with CNTs closely and uniformly. The close and uniform structure is beneficial for promoting the decomposition of Na_2CO_3 and CNTs in proper voltage range (< 3.8 V).

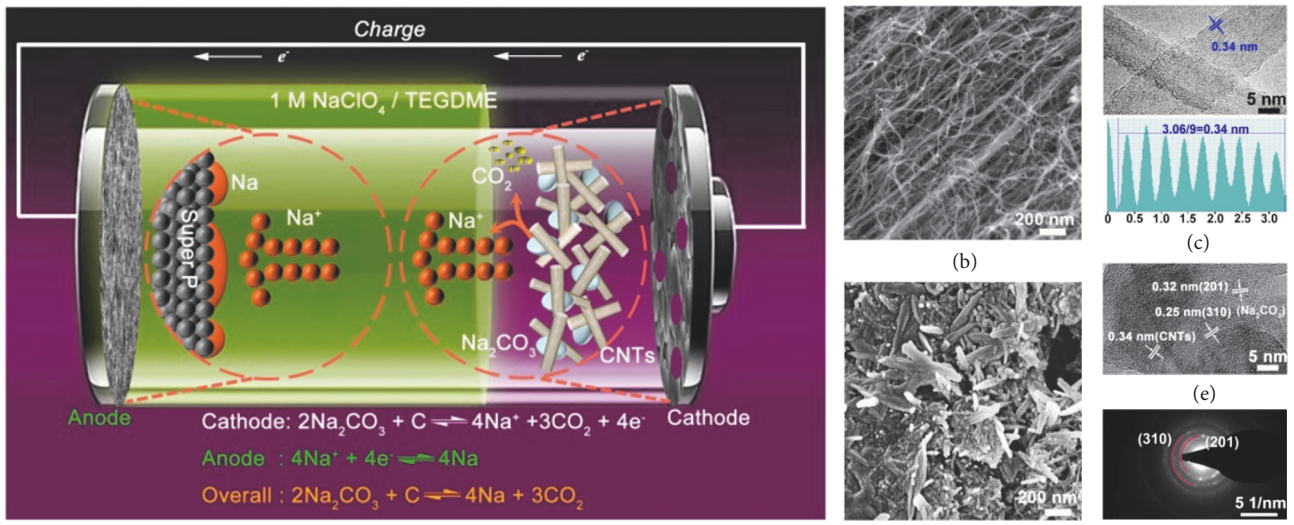


FIGURE 1: **The structure of rechargeable Na-CO_2 batteries. (a)** The scheme of Na-CO_2 batteries starting from Na_2CO_3 and CNTs. SEM **(b)** and HRTEM **(c)** images of pristine CNTs with lattice distance of 0.34 nm. SEM **(d)** and HRTEM **(e)** images of prepared Na_2CO_3/CNTs composites. **(f)** The corresponding SAED pattern of **(e)**.

The anode is Super P/Al, which can effectively reduce the generation of Na dendrite and increase the Coulombic efficiency of the batteries because of the large specific surface area and low nucleation barrier for Na plating. The optimized electrolyte is 1 M $NaClO_4$-tetraethylene glycol dimethyl ether (TEGDME) in view of its high voltage window (> 4.8 V versus Na^+/Na) and high ionic conductivity (0.18 S m^{-1}) (Figure S1). By means of various characterizations such as in situ Raman, gas chromatograph (GC), in situ optical microscopy, and nuclear magnetic resonance (NMR), we demonstrate that the charging reaction is $2Na_2CO_3 + C \longrightarrow 4Na + 3CO_2$ without any side reactions. After optimization, the dendrite-free Na-CO_2 batteries show a relatively long cycling life (100 cycles) with cut-off capacity of 0.3 mAh cm^{-2}. Remarkably, the pouch-type Na-CO_2 batteries starting from Na_2CO_3 and CNTs deliver a total energy density of 183 Wh kg^{-1} (based on the whole mass of the pouch-type batteries, 4 g).

2. Results

2.1. Preparation of Na_2CO_3/CNTs Composite. To ensure the decomposition of cathode (Na_2CO_3 and carbon) under low voltage range, there are two key points which should be addressed properly. One is the combination status of Na_2CO_3 and carbon. The other is the carbon source, which acts as the conductive base and the reactant to participate in the charging reaction.

To guarantee uniform and close combination of Na_2CO_3 and carbon, we prepared the composites of Na_2CO_3 and carbon by a facile dissolution-crystallization method (Figure S2) [25]. The commercial CNTs have a porous cross-linking structure with the wall thickness of about 5 nm and spacing layers of 0.34 nm (Figures 1(b) and 1(c)). The outer walls of CNTs offer spaces for Na_2CO_3 to nucleate and anchor. Meanwhile, the inner walls act as conductive networks to promote electron transport easily [26, 27]. After the dissolution-crystallization process, we got the Na_2CO_3/CNTs composite, in which the stick-shaped Na_2CO_3 (about 200-300 nm in length) are intertwined with CNTs closely and uniformly (Figure 1(d)). Through the HRTEM images and the selected area electron diffraction (SAED), we can see the (201) and (310) planes of Na_2CO_3 and multiwall structure of CNTs in the composite (Figures 1(e) and 1(f)). In addition, we find that Na_2CO_3 crystal only grows on the outer walls of CNTs (Figure S3). The reason for this phenomenon is that the CNTs have less polarity and belong to superhydrophobic materials [28, 29]. There are some defects with hydrophilic groups (-OH, -COOH) in the outer wall of the CNTs, which is conducive to the nucleation and crystallization of water-soluble Na_2CO_3 on the outer walls of CNTs [30, 31]. However, the hydrophobicity of the inner walls prevents the water from entering.

We also used the same fabricating method to explore another four kinds of carbon materials, including reduced graphene oxide, Super P, single-walled carbon nanotubes, and double-walled carbon nanotubes. We finally chose multi-walled carbon nanotubes as the carbon source due to its high electrical conductivity, cross-linking structure, and suitable defects (optimization details can be seen in Supporting Information, Figures S4-6).

2.2. Decomposition of Na_2CO_3/CNTs Cathode. After obtaining the Na_2CO_3/CNTs composite, we investigate the decomposition issue of Na_2CO_3/CNTs cathode by using Super P/Al as anode (the detailed optimization of anode can be seen in Figures S7-9). In this part, we first optimized the content of Na_2CO_3 in the cathode and then revealed the charging mechanism thoroughly. The powder X-ray diffraction

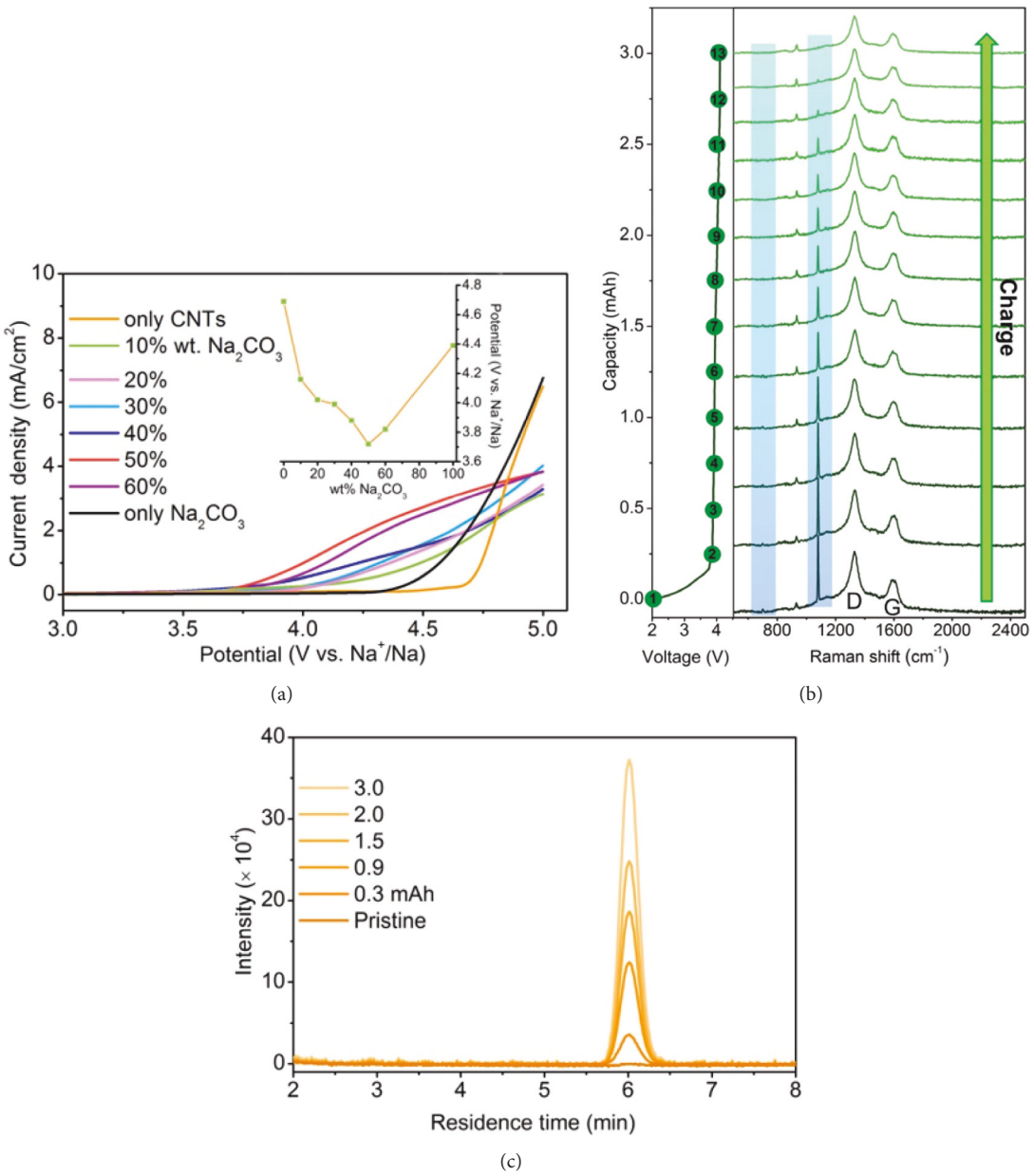


FIGURE 2: **Decomposition of Na_2CO_3/CNTs cathode on charging process. (a)** LSVs of pure CNTs, 10%, 20%, 30%, 40%, 50%, and 60% weight ratio of Na_2CO_3 in Na_2CO_3/CNTs cathodes, and pure Na_2CO_3 with titanium powder (titanium powder acts as conductive additive) at the sweep rate of 1 mV s^{-1}. The inset in **(a)** is the initial decomposition voltages of various cathodes. **(b)** The galvanostatic charge curve at 0.1 mA cm^{-2} with 13 selected points and corresponding in situ Raman spectra. **(c)** Evolution of CO_2 characterized by GC.

(XRD) patterns of pure CNTs, Na_2CO_3, and as-prepared Na_2CO_3/CNTs cathodes with different mass ratios are shown in Figure S10A. All diffraction peaks of pure Na_2CO_3 are well indexed with the standard XRD pattern of Na_2CO_3 (PDF no. 19-1130). In the XRD pattern of CNTs, a broad peak at 26.4° is assigned to the (002) crystal face. When the mass percentage of Na_2CO_3 in the cathodes is low (10, 20, and 30 wt%), there are no apparent diffraction peaks of Na_2CO_3, indicating that Na_2CO_3 are coated by CNTs. When the mass percentage of Na_2CO_3 further increases (40, 50, and 60 wt%), diffraction peaks of Na_2CO_3 emerge and gradually increase, which suggests that the grain size of Na_2CO_3 becomes large [32]. Due to the insulting properties of Na_2CO_3, charge transfer resistance of Na_2CO_3/CNTs cathodes becomes larger and larger when the mass percentage of Na_2CO_3 gradually increases (Figure S10B). When the mass percentage of Na_2CO_3 increases to 60 wt%, there is a jump in the impedance value, indicating that the content of Na_2CO_3 is too much to form uniform mixture.

Then, we explore the decomposition behavior of cathodes with different percentage of Na_2CO_3 by linear sweep voltammetry (LSV, Figure 2(a)). The results show that the

decomposition voltages reduce first and then increase with the increased content of Na_2CO_3 in cathodes (the inset in Figure 2(a)). This result could be attributed to the following reasons. First, when there are only pure CNTs or Na_2CO_3, the charge reaction lacks another reactant, leading to a high charging voltage and resulting in the decomposition of the electrolyte. Note that we added 90 wt% titanium powders as conductive additive when we investigated the decomposition of pure Na_2CO_3 (Figure S11). Second, most of Na_2CO_3 are coated with CNTs when the content of Na_2CO_3 is low, so the electrolyte is difficult to spread to the surface of Na_2CO_3. When the amount of Na_2CO_3 increases to high value (60 wt%), the large particles of Na_2CO_3 cannot mix well with CNTs, resulting in poor conductivity. Therefore, a minimum decomposition voltage would be achieved when the content of Na_2CO_3 is intermediate. Here, a minimum decomposition voltage of 3.72 V was achieved when the content of Na_2CO_3 is 50 wt%, which should be originated from the best three-phase interface and the most uniform mixing degree with this content. In addition, the charge tests of cathodes were carried out, and the results are consistent with the LSV curves (Figure S12).

The interaction between Na_2CO_3 and CNTs in cathode is confirmed by X-ray photoelectron spectroscopy (XPS) (Figure S13). Compared with pure Na_2CO_3, the C1s spectra of CO_3^{2-} in cathode shifted to the lower binding energy, indicating that the C atoms on the CNTs interact with the O atoms on the CO_3^{2-} [33]. Meanwhile, the O atoms in the CO_3^{2-} also reduce the strength of C-C on the CNTs, resulting in a new C-C peak at the 283.47 eV [34].

After optimizing the Na_2CO_3/CNTs cathode, we studied the charging mechanism through several methods. We first designed an in situ Raman coin cell with a 2 mm observation hole in the cathode cap to collect Raman signals from cathode in real time (Figure S14). Thirteen points were selected on charge profiles. As shown in Figure 2(b), the main peaks at 1080 and 700 cm^{-1} corresponding to Na_2CO_3 decrease little by little during charging process. In addition, the intensity of G and D band corresponding to CNTs also gradually decreases. The results indicate that the cathode can decompose in charging process.

Moreover, we employed gas chromatography (GC) measurements to monitor the gas generation during the charging process in pure argon atmosphere (1 atm) (Figure 2(c)). The results show that CO_2 generates throughout the charging process. The retention time of CO_2 in GC column is 6 minutes and no other new gases were detected. The practical evolution concentration of CO_2 is 3.39×10^4 ppm, which corresponds to 7.845×10^{-5} mol. This value is less than the theoretical one with 3.63×10^4 ppm (8.393×10^{-5} mol, and detailed calculations can be found in the Supporting Information). The difference can probably be attributed to the reasons that CNTs has strong adsorption effect on CO_2. In addition, CO_2 also show certain solubility in TEGDME solvent [4, 35]. In order to prove that the CO_2 is not produced by side reactions, we confirmed the components of electrolyte after charge by ^1H and ^{13}C NMR spectroscopy. The ^1H and ^{13}C NMR spectroscopy of the electrolyte have not changed after charge (Figure S15), indicating that the electrolyte did not decompose during the charging process.

We also characterized the morphological features of the cathode after charge by SEM (Figure S16). The results show that the surface of cathode becomes porous and the stick Na_2CO_3 disappears at the end of the charge process. The specific surface area of the cathode also increased from 27.498 $m^2\ g^{-1}$ to 215.52 $m^2\ g^{-1}$ after charge process (Figure S17). In the pristine cathode, Na_2CO_3 closely combined with carbon nanotubes (Figures S4A and S4B), resulting in a dense electrode. After charging, all the Na_2CO_3 are decomposed, and the original position of Na_2CO_3 is vacated. In addition, the carbon nanotube skeleton is well maintained (Figure S16). Therefore, the cathode becomes loose and porous, resulting in a significant increase in specific surface area. Furthermore, the charge transfer resistance (diameter of the semicircle) of the batteries also significantly reduced after full charge (Figure S18), indicating that the nonconductive Na_2CO_3 decomposed.

2.3. Na Generation. Combining the Super P/Al anode and optimized Na_2CO_3/CNTs cathode, we construct full batteries to characterize the generation of Na. SEM images of the pristine Super P/Al anode show that Super P with diameter of 30 nm are coated on the surface of Al (Figure 3(a) and Figure S19). Compared with the pristine anode, the electrode surface is covered by silver-white charging products after charging to 1 mAh (Figure 3(b)). XRD pattern of the charging products is shown in Figure 3(c). The peaks at 29.3°, 42.1°, and 52.2° are well matched with the (110), (200), and (211) crystal faces of Na (PDF no. 22-948), respectively. It can be seen from SEM images (Figure S20) that the metal Na has a smooth surface and disperses evenly, indicating that Super P plays a role in dispersing current density. The yield of Na is directly proportional to the charging capacity (1-3 mAh, Figure S21). When the charging capacity increased to 3 mAh, the surface of Super P was covered with a layer of Na.

In order to further observe the process of Na generation more visually, we designed an in situ optical microscopy setup to monitor the change of anode during charge process in real time (Figure 3(d)). The in situ optical microscopy setup includes an Au anode, a Na_2CO_3/CNTs cathode, a seal ring for sealing electrolyte, and an optics lens. We collected optical microscope images of the Au anode during the charge process at the sweep rate of 0.2 mV s^{-1} (Figure S22). Figure 3(e) shows a series of light-field optical microscope images, which successively present the morphology evolution of the Au electrode. The pristine Au electrode is clean and flat before charge voltage of 3.7 V (0 s). With the charging time going on, the surface of Au electrode gradually becomes dark (60 s). The XRD patterns (Figure S23) of Au electrode prove that the dark materials are metal Na. The entire surface of the Au electrode was covered by generated Na after 300 s. With further increase of charging depth, more Na deposited and covered the electrode layer by layer (480s, 720s, and 1020s). A video of Na deposition process can be seen in Movie S1. Moreover, we measured the surface height of Au electrode before and after charge through atomic force microscope (AFM) (Figure 3(f)). After charging for 2040 s, the height of

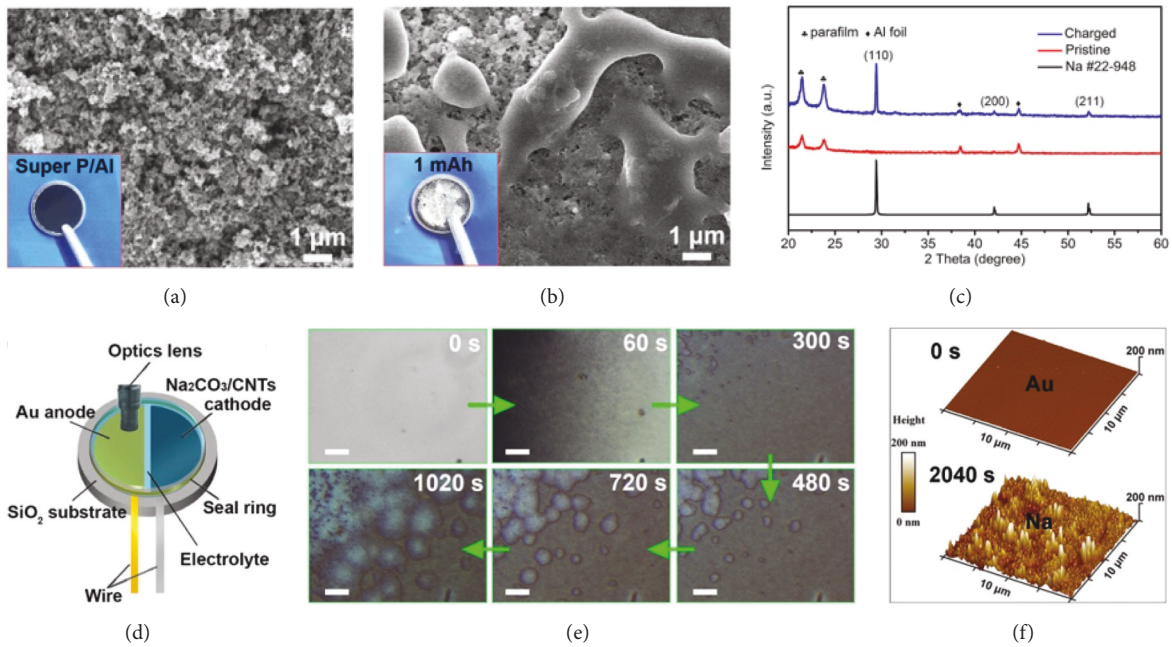


FIGURE 3: **Generation of Na on anode.** SEM images of **(a)** pristine Super P/Al anode and **(b)** the Super P/Al anode after charging to 1 mAh with Na coated on the surface. The insets in **(a)** and **(b)** are the corresponding photographs of the anode. **(c)** XRD patterns of Super P/Al anode before and after charge. **(d)** Schematic diagram of in situ optical microscope setup in liquid electrolyte. **(e)** In situ optical images for the process of Na formation. **(f)** AFM images of Na deposition on Au electrode at the time of 0 s and 2040 s. Scale bar: 40 μm.

Au electrode increases to 200 nm, indicating the thickness of deposited metal Na layer. These results demonstrate that the charging process accords with the following equation: $2Na_2CO_3 + C \longrightarrow 4Na + 3CO_2$.

2.4. Electrochemical Performance. After revealing the mechanism, we evaluate the electrochemical performance of the Na-CO_2 batteries without preloaded metal Na in CO_2 atmosphere (1 atm). The batteries firstly charged to produce Na. The voltage profile displays a flat plateau before charging to 4.6 mAh cm^{-2} (Figure S24), indicating that Na_2CO_3 and CNTs can decompose at low voltage. At the end of the charge process, the voltage curve starts to go up, demonstrating that all the Na_2CO_3 have almost broken down. The batteries show a maximal capacity of 5 mAh cm^{-2}, which is very close to the theoretical value (calculation details can be seen in Supplementary Materials).

Subsequently, we evaluate cycling performance of the batteries at different current densities with the limited capacity at 0.3 mAh cm^{-2}. At a current density of 0.05 mA cm^{-2}, the charge potential of the batteries was maintained below 4 V after 100 cycles (Figure 4(a)). The results demonstrate an impressive stability of Na-CO_2 batteries. As the current density increased to 0.10 and 0.15 mA cm^{-2}, the batteries were capable of discharging/charging for over 50 cycles (Figures S25A and S25B). The excellent performance of the batteries shows that the Na generated by decomposition of Na_2CO_3 and CNTs can be used effectively. The surface morphology of Na coated Super P/Al anode after 50 cycles was studied by SEM (Figure S26). It can be seen that the Na covered surface of Super P/Al anode remains smooth and no Na dendrite is discovered, which suggests a uniform deposition/stripping process of Na on the surface of Super P/Al anode.

The morphological features of discharge products at different current densities were observed by SEM. We find that the current densities could affect the morphologies of the discharge products. As shown in Figure 4(b), round-shaped discharge products (~ 100 nm) form when the current density is 0.05 mA cm^{-2}. As the current densities rise (0.10 and 0.15 mA cm^{-2}), the discharge products become larger with rectangle shape (~ 200 nm) at 0.10 mA cm^{-2} and nanorod shape (~ 500 nm) at 0.15 mA cm^{-2} (Figures S27A and S27B). The changes in the morphology of the discharge products are similar to previous report [4]. Although the morphology of discharge products is different, we prove that Na_2CO_3 appear in all discharge products at different current densities through Raman characterization (the insets of Figure 4(b), Figures S27A and S27B). According to our previous work, the other discharge product is amorphous carbon that is mixed with sodium carbonate [3, 4].

We further fabricate pouch-type Na-CO_2 batteries to assess their potential applications in energy storage. The pouch-type batteries are composed of Super P/Al (anode), Na_2CO_3/CNTs (cathode), and Celgard (separator) soaked in electrolyte (Figure 4(c) and Figure S28). During the charging process, the sodium ions are removed from Na_2CO_3 and in situ reduced to metal Na on the Super P/Al anode. When the charging process finished, the open circuit voltage of the batteries is 2.35 V (Figure 4(d)), which is consistent with the voltage of the common Na-CO_2 batteries with preloaded metal Na. The pouch-type Na-CO_2 batteries can light a LED bulb with 1 watt (Figure 4(e)). Movie S2 is a video of the

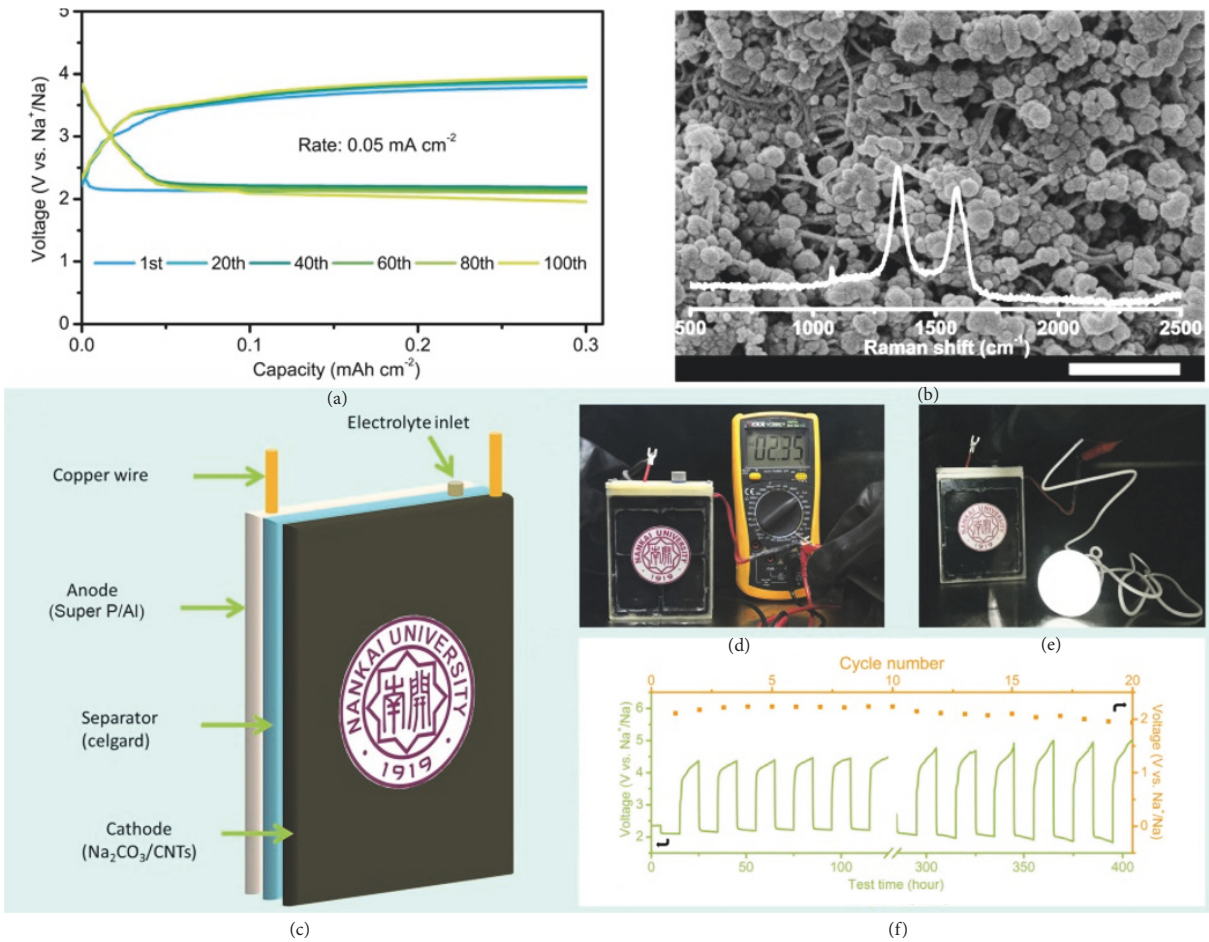


FIGURE 4: **Electrochemical performance of Na-CO_2 batteries without preloaded metal Na in pure CO_2 atmosphere with pressure of 1 atm. (a)** The cycling stability of Na-CO_2 batteries with a cut-off capacity of 0.3 mAh cm^{-2} at current densities of 0.05 mA cm^{-2}. **(b)** SEM images of the discharge products after first discharge process at the rate of 0.05 mA cm^{-2}. The inset in **(b)** is the corresponding Raman spectrum. **(c)** Schematic illustration of the cell configuration composed of anode (Super P/Al), separator (Celgard), and cathode (Na_2CO_3/CNTs). **(d)** A digital photo of package battery with an open circuit voltage of 2.35 V. **(e)** A digital photo of package battery powering one-watt (1 W) light bulbs. **(f)** Cycling performance with a reversible capacity of 100 mAh at a current of 10 mA. Scale bar: 500 nm.

process that bulb is lit up. With cut-off voltage at 1.9 V, the initial discharge capacity of 350 mAh can be obtained at a current of 10 mA (Figure S29), corresponding to an energy density of 183 Wh kg^{-1} based on the whole mass of the pouch-type batteries (4 g). The energy density of the pouch-type Na-CO_2 batteries is higher than that of commercial Li-ion batteries (150-180 Wh kg^{-1}) [36]. The pouch-type Na-CO_2 batteries exhibit stable cycling performance with an average discharge voltage of 2.13 V (Figure 4(f)). The results indicate the possibility of practical applications of Na-CO_2 batteries which start from Na_2CO_3 and CNTs.

3. Discussion

In conclusion, we have successfully constructed dendrite-free rechargeable Na-CO_2 batteries without preloaded metal Na. The batteries operate in pure CO_2 atmosphere, consisting of Na_2CO_3/CNTs cathode, Super P/Al anode, and $NaClO_4$/TEGDME electrolyte. The uniform Na_2CO_3/CNTs cathode with 50 wt% Na_2CO_3 could decompose under 3.8 V during the charge process. The Super P/Al anode is beneficial for dendrite-free Na plating/stripping (0.5 mAh cm^{-2}, 100 cycles), showing higher and steadier Coulombic efficiency (98%) than that of pure Al anode. Combination of in situ Raman, GC, in situ optical microscopy, XRD, and NMR demonstrates that Na generate in the Super P/Al anode, and CO_2 release in Na_2CO_3/CNTs cathode without any side reactions during initial charge process. The charging reaction could be described as $2Na_2CO_3 + C \longrightarrow 4Na + 3CO_2$. Due to effective use of the generated Na, the coin-type batteries are capable of charging/discharging for 100 cycles with a cut-off capacity of 0.3 mAh cm^{-2}. Moreover, the pouch-type batteries deliver a large energy density of 183 Wh kg^{-1}. Our work paves the way to construct safe and cheap Na-CO_2 batteries without preloaded metal Na for practical energy storage applications.

4. Materials and Methods

4.1. Electrolyte Treatment. Tetraethylene glycol dimethyl ether (TEGDME) (Aladdin) is stilled by reduced pressure distillation method and stored with freshly activated molecular sieves (type 4 Å, beads 8-12 mesh, J&K). $NaClO_4$ (anhydrous, Alfa Aesar) and $NaCF_3SO_3$ (anhydrous, Aladdin) are dried in a vacuum oven at 80°C for 24 hours before use. The electrolyte solutions of 1 M $NaClO_4$/TEGDME and 1 M $NaCF_3SO_3$/TEGDME are prepared in a glove box filled with high-purity argon (O_2 and H_2O < 1 ppm).

4.2. Na_2CO_3/CNTs Cathode Preparation. In a typical preparation process, 50 mg commercial Na_2CO_3 and 40 mg CNTs dissolved in a mixed solvent including 4 mL ethanol and 4 mL water (1:1, v/v) under sonication for 2 hours. Then the solution was transferred to a culture dish and ultrasonic heated until solvent evaporation at 80°C. During the solvent volatilization process, Na_2CO_3 recrystallized and deposited on the surface of CNTs. After full evaporation of solvent, black Na_2CO_3/CNTs composite powder was obtained. The powder was characterized by XRD, XPS, SEM, and TEM. Then we rolled piece with Na_2CO_3/CNTs composite powder (90 wt%) and PTFE solution as binder (10 wt%), followed by drying in a vacuum oven at 80°C for 12 hours. Every piece weighs about 10~30 mg with a diameter of 14 mm. The other cathodes were prepared in the same way.

4.3. Super P/Al Anode Preparation. Conductive carbon black (TIMCAL Super P li) and polyvinylidene fluoride (PVDF) (9:1) were mixed with *N*-methylpyrrolidone (NMP). Slurry was then doctor bladed onto Al foil, followed by drying in a vacuum oven at 100°C for 10 hours to obtain Super P/Al anode with Super P mass loading of ~0.2 mg/cm^2.

4.4. Batteries Assembly. In order to optimize the anode, the Na-Al or Na-Super P/Al batteries were assembled by stacking a metal sodium (12 mm in diameter), Celgard separator (16 mm in diameter) soaked with 60 μL of electrolyte, and a Al foil or Super P/Al electrodes (14 mm in diameter) successively in a CR2032 coin-type battery. The full cells were also assembled in CR2032 coin cells with Super P/Al anode, Celgard separator soaked with 80 μL of electrolyte, and the as-prepared Na_2CO_3/CNTs cathode. A hole is drilled in the cathode shell (4 mm in diameter) so that the CO_2 can easily and quickly pass the cathode. Then, the battery is placed in a bottle filled with pure CO_2 atmosphere. Pouch-type full cells are made up of one plastic case (8 × 9 cm^2), a Super P/Al anode (7 × 6.8 cm^2, 0.25 g), a piece of Celgard (8 × 7 cm^2) with 2 mL electrolyte, and a Na_2CO_3/CNTs cathode (6 × 5.1 cm^2, 1.6 g). The total mass of this pouch-type battery is 4 g. The pouch-type full cells run in a glove box with pure CO_2 atmosphere.

Data Availability

All data needed to evaluate the conclusions in the paper are present in the paper and/or the Supplementary Materials. Additional data related to this paper may be requested from the authors.

Conflicts of Interest

The authors declare no competing financial interests.

Authors' Contributions

Jianchao Sun and Jun Chen conceived this project. Jianchao Sun and Hao Yang designed experimental procedures in detail. Jianchao Sun., Mo Han, and Lianyi Shao performed the characterization and data analysis. Jianchao Sun, Yong Lu, and Jun Chen cowrote the paper. Jun Chen directed the research.

Acknowledgments

This work was supported by the National Programs for Nano Key Project (2016YFA0202500), the Ministry of Education (B12015), and Tianjin Key Project (16PTSYJC00030).

Supplementary Materials

Figure S1. The electrochemical stability window and ionic conductivity of electrolyte. Figure S2. Schematic diagram of the fabrication process of Na_2CO_3/CNTs composites. Figure S3. TEM images of Na_2CO_3/CNTs cathode. Figure S4. The morphology characterization of various cathodes with different carbon sources and the comparision of charge voltage. Figure S5. Characterization of raw Na_2CO_3. Figure S6. The comparision of different carbon nanotubes. Figure S7. The optimized anode. Figure S8. Comparison of the sodium nucleation overpotential for Super P/Al and bare Al current collectors. Figure S9. SEM images of Na deposition (3 mAh) at different anodes. Figure S10. The optimization of Na_2CO_3/CNTs composites. Figure S11. EIS of mixed materials consisting of Na_2CO_3 and titanium powder (mass ratio of 1: 9). Figure S12. The charge profiles of pure CNTs, Na_2CO_3/CNTs, and pure Na_2CO_3 with titanium powder at current density of 0.1 mA cm^{-2}. Figure S13. The X-ray photoelectron spectroscopy (XPS) of pure CNTs, pure Na_2CO_3 and Na_2CO_3/CNTs composites cathode of 50 wt% Na_2CO_3 content. Figure S14. The in-situ Raman battery. Figure S15. ^{1}H NMR and ^{13}C NMR spectra of electrolyte before and after charge. Figure S16. SEM images of Na_2CO_3/CNTs cathode after charge. Figure S17. The specific surface area (BET) of cathode. Figure S18. EIS of the battery before and after charge. Figure S19. SEM images of pristine Super P/Al anode. Figure S20. SEM images of Super P/Al electrode after charge. Figure S21. The photographs of Super P/Al anode with different charging capacity (0-3 mAh). Figure S22. A representative LSV curve of Na deposition in the in-situ tests with Na_2CO_3/CNTs as working electrode and Au as counter electrode. Figure S23. XRD patterns of the deposited Na on the Au electrode. Figure S24. The full charge profile of Na-CO_2 batteries with 5 mAh cm^{-2} at 0.1 mA cm^{-2}. Figure S25. The cycling stability of Na-CO_2 batteries with a cut-off capacity of 0.3 mAh cm^{-2} at different current densities.

Figure S26. SEM images of Na coated Super P/Al anode after 50 cycles, exhibiting a smooth surface. Figure S27. SEM images of the discharge products after first discharge process at different rates of (A) 0.10 mA cm^{-2} and (B) 0.15 mA cm^{-2}. Figure S28. Photographs of Super P/Al anode and Na_2CO_3/CNTs cathode. Figure S29. Pouch-type battery performance. movie S1. Sodium deposition process. movie S2. Process that bulb is be lit up. References [37], [38], [31], [39]. *(Supplementary Materials)*

References

[1] S. K. Das, S. Xu, and L. A. Archer, "Carbon dioxide assist for non-aqueous sodium-oxygen batteries," *Electrochemistry Communications*, vol. 27, pp. 59–62, 2013.

[2] S. Xu, Y. Lu, H. Wang, H. D. Abruña, and L. A. Archer, "A rechargeable Na–CO_2/O_2 battery enabled by stable nanoparticle hybrid electrolytes," *Journal of Materials Chemistry A*, vol. 2, no. 42, pp. 17723–17729, 2014.

[3] X. Hu, J. Sun, Z. Li, Q. Zhao, C. Chen, and J. Chen, "Rechargeable room-temperature Na-CO_2 batteries," *Angewandte Chemie International Edition*, vol. 55, no. 22, pp. 6482–6486, 2016.

[4] X. Hu, Z. Li, Y. Zhao et al., "Quasi–solid state rechargeable Na-CO_2 batteries with reduced graphene oxide Na anodes," *Science Advances*, vol. 3, no. 2, p. e1602396, 2017.

[5] W. Luo, C. Lin, O. Zhao et al., "Ultrathin surface coating enables the stable sodium metal anode," *Advanced Energy Materials*, vol. 7, no. 2, p. 1601526, 2017.

[6] S. Choudhury, S. Wei, Y. Ozhabes et al., "Designing solid-liquid interphases for sodium batteries," *Nature Communications*, vol. 8, no. 1, 2017.

[7] H. Yadegari, Q. Sun, and X. Sun, "Sodium-oxygen batteries: a comparative review from chemical and electrochemical fundamentals to future perspective," *Advanced Materials*, pp. 7065–7093, 2016.

[8] V. Palomares, P. Serras, I. Villaluenga, K. B. Hueso, J. Carretero-González, and T. Rojo, "Na-ion batteries, recent advances and present challenges to become low cost energy storage systems," *Energy & Environmental Science*, vol. 5, no. 3, pp. 5884–5901, 2012.

[9] S. R. Gowda, A. Brunet, G. M. Wallraff, and B. D. McCloskey, "Implications of CO_2 contamination in rechargeable nonaqueous Li-O_2 batteries," *The Journal of Physical Chemistry Letters*, vol. 4, no. 2, pp. 276–279, 2013.

[10] Y.-C. Lu, E. J. Crumlin, T. J. Carney et al., "Influence of hydrocarbon and CO_2 on the reversibility of Li-O_2 chemistry using in situ ambient pressure X-ray photoelectron spectroscopy," *The Journal of Physical Chemistry C*, vol. 117, no. 49, pp. 25948–25954, 2013.

[11] T. Zhang and H. Zhou, "A reversible long-life lithium–air battery in ambient air," *Nature Communications*, vol. 4, no. 1, 2013.

[12] S. Meini, N. Tsiouvaras, K. U. Schwenke et al., "Rechargeability of Li-air cathodes pre-filled with discharge products using an ether-based electrolyte solution: implications for cycle-life of Li-air cells," *Physical Chemistry Chemical Physics*, vol. 15, no. 27, pp. 11478–11493, 2013.

[13] C. Ling, R. Zhang, K. Takechi, and F. Mizuno, "Intrinsic barrier to electrochemically decompose Li_2CO_3 and LiOH," *The Journal of Physical Chemistry C*, vol. 118, no. 46, pp. 26591–26598, 2014.

[14] F. Cheng and J. Chen, "Something from nothing," *Nature Chemistry*, vol. 4, no. 12, pp. 962-963, 2012.

[15] Y. Zhang, Q. Cui, X. Zhang et al., " Amorphous Li ," *Angewandte Chemie*, vol. 128, no. 36, pp. 10875–10879, 2016.

[16] Z. Chang, J. Xu, and X. Zhang, "Recent Progress in Electrocatalyst for Li-O_2 batteries," *Advanced Energy Materials*, vol. 7, no. 23, p. 1700875, 2017.

[17] Y. Li, Q. An, Y. Cheng et al., "A high-voltage rechargeable magnesium-sodium hybrid battery," *Nano Energy*, vol. 34, pp. 188–194, 2017.

[18] Z. Zhu, F. Cheng, and J. Chen, "Investigation of effects of carbon coating on the electrochemical performance of $Li_4Ti_5O_{12}$/C nanocomposites," *Journal of Materials Chemistry A*, vol. 1, no. 33, pp. 9484–9490, 2013.

[19] Y. A. Kim, M. Kojima, H. Muramatsu et al., "In situ Raman study on single- and double-walled carbon nanotubes as a function of lithium insertion," *Small*, vol. 2, no. 5, pp. 667–676, 2006.

[20] Y.-S. Hu, P. Adelhelm, B. M. Smarsly, S. Hore, M. Antonietti, and J. Maier, "Synthesis of hierarchically porous carbon monoliths with highly ordered microstructure and their application in rechargeable lithium batteries with high-rate capability," *Advanced Functional Materials*, vol. 17, no. 12, pp. 1873–1878, 2007.

[21] S. Chou and Y. Yu, "Next generation batteries: aim for the future," *Advanced Energy Materials*, vol. 7, no. 24, p. 1703223, 2017.

[22] Y. Zhao, L. V. Goncharova, A. Lushington et al., "Superior stable and long life sodium metal anodes achieved by atomic layer deposition," *Advanced Materials*, vol. 29, no. 18, p. 1606663, 2017.

[23] A. P. Cohn, N. Muralidharan, R. Carter, K. Share, and C. L. Pint, "Anode-free sodium battery through in situ plating of sodium metal," *Nano Letters*, vol. 17, no. 2, pp. 1296–1301, 2017.

[24] M. D. Tikekar, S. Choudhury, Z. Tu, and L. A. Archer, "Design principles for electrolytes and interfaces for stable lithium-metal batteries," *Nature Energy*, vol. 1, no. 9, p. 16114, 2016.

[25] H. J. Kitchen, S. R. Vallance, J. L. Kennedy et al., "Modern microwave methods in solid-state inorganic materials chemistry: from fundamentals to manufacturing," *Chemical Reviews*, vol. 114, no. 2, pp. 1170–1206, 2014.

[26] X. Hu, Z. Li, and J. Chen, "Flexible Li-CO_2 batteries with liquid-free electrolyte," *Angewandte Chemie International Edition*, vol. 56, no. 21, pp. 5785–5789, 2017.

[27] Y. Liang, H. Wang, P. Diao et al., "Oxygen reduction electrocatalyst based on strongly coupled cobalt oxide nanocrystals and carbon nanotubes," *Journal of the American Chemical Society*, vol. 134, no. 38, pp. 15849–15857, 2012.

[28] S. Li, H. Li, X. Wang et al., "Super-hydrophobicity of large-area honeycomb-like aligned carbon nanotubes," *The Journal of Physical Chemistry B*, vol. 106, no. 36, pp. 9274–9276, 2002.

[29] Y. Liu, J. Tang, R. Wang et al., "Artificial lotus leaf structures from assembling carbon nanotubes and their applications in hydrophobic textiles," *Journal of Materials Chemistry*, vol. 17, no. 11, pp. 1071–1078, 2007.

[30] E. T. Thostenson, Z. Ren, and T.-W. Chou, "Advances in the science and technology of carbon nanotubes and their composites: a review," *Composites Science and Technology*, vol. 61, no. 13, pp. 1899–1912, 2001.

[31] J.-C. Charlier, "Defects in carbon nanotubes," *Accounts of Chemical Research*, vol. 35, no. 12, pp. 1063–1069, 2002.

[32] C. Guo, K. Zhang, Q. Zhao, L. Pei, and J. Chen, "High-performance sodium batteries with the 9,10-anthraquinone/

CMK-3 cathode and an ether-based electrolyte," *Chemical Communications*, vol. 51, no. 50, pp. 10244–10247, 2015.

[33] V. Chauvaut, E. Duval, B. Malinowska, M. Cassir, and P. Marcus, "XPS study of titanium species exposed to molten Li_2CO_3-Na_2CO_3 in the anodic conditions used in molten carbonate fuel cells," *Journal of Materials Science*, vol. 34, no. 9, pp. 2015–2022, 1999.

[34] C. Morant, J. Andrey, P. Prieto, D. Mendiola, J. M. Sanz, and E. Elizalde, "XPS characterization of nitrogen-doped carbon nanotubes," *Physica Status Solidi (a)—Applications and Materials Science*, vol. 203, no. 6, pp. 1069–1075, 2006.

[35] Z. Xie, X. Zhang, Z. Zhang, and Z. Zhou, "Metal-CO_2 batteries on the road: CO_2 from contamination gas to energy source," *Advanced Materials*, vol. 29, no. 15, p. 1605891, 2017.

[36] B. Dunn, H. Kamath, and J. M. Tarascon, "Electrical energy storage for the grid: a battery of choices," *Science*, vol. 334, no. 6058, pp. 928–935, 2011.

[37] S. A. Freunberger, Y. Chen, N. E. Drewett, L. J. Hardwick, F. Bardé, and P. G. Bruce, "The lithium-oxygen battery with ether-based electrolytes," *Angewandte Chemie International Edition*, vol. 50, no. 37, pp. 8609–8613, 2011.

[38] A. C. Luntz and B. D. McCloskey, "Nonaqueous Li-air batteries: a status report," *Chemical Reviews*, vol. 114, no. 23, pp. 11721–11750, 2014.

[39] N. Song, H. Liu, and J. Fang, "Fabrication and mechanical properties of multi-walled carbon nanotube reinforced reaction bonded silicon carbide composites," *Ceramics International*, vol. 42, no. 1, pp. 351–356, 2016.